Fabrication of ZnO/SiO$_2$ and SiO$_2$/α-Zn$_2$SiO$_4$ composites with dye adsorption and antimicrobial properties

Hendris Hendarsyah Kurniawan[1], Novita Ariani[1], Andreas Andreas[1], Aspiyanto Aspiyanto[1], Nur Tjahyo Eka Darmayanti[2], Qudsiyyatul Lailiyah[2], Oman Zuas[2,*], Muhammad Iqbal Syauqi[3], Toto Sudiro[4]

[1]*Research Centre for Chemistry (RCC), National Research and Innovation Agency (BRIN), KST BJ Habibie, Serpong Tangerang Selatan, Banten, 15314, Indonesia*

[2]*Research Centre for Testing Technology and Standard (PRTPS), National Research and Innovation Agency (BRIN), KST BJ Habibie, Serpong Tangerang Selatan, Banten, 15314, Indonesia*

[3]*Department of Chemistry, Faculty of Mathematics and Natural Sciences, Universitas Indonesia, Depok 16424, Indonesia*

[4]*Research Centre for Advanced Material (RCAM), National Research and Innovation Agency (BRIN), KST BJ Habibie, Serpong Tangerang Selatan, Banten, 15314, Indonesia*

Abstract

Zinc-silicon oxide composites were fabricated using direct precipitation. Sodium silicate isolated from rice husk ash and commercial zinc nitrate were used as starting materials. The as-prepared Zn-Si oxide composites were then subjected to two separate treatments: one without calcination (as-prepared sample, APS) and another with calcination at 1000 °C (calcined sample, CS). The obtained samples were characterized using TGA-DSC, XRD, FT-IR, UV-DRS, PL spectroscopy, TEM and FESEM. The electron microscopy analysis confirmed that APS is in the form of ZnO/SiO$_2$ with pseudo-amorphous particle shape, whereas CS consists of SiO$_2$/α-Zn$_2$SiO$_4$ structure having interconnected fused-like particles with improved crystallinity. These results were in good agreement with XRD and FT-IR data. Additionally, the enhanced crystallinity of the CS led to a decrease in the absorption intensity of UV-DRS and an increase in its PL intensity. Activity studies revealed that the APS demonstrated better adsorption efficiency for Congo red removal but lesser antibacterial efficacy than the CS. It has been suggested that the surface and particle architectures of both APS and CS govern their activity performance.

Keywords: Zn-Si oxide composite, rice husk ash, precipitation, structural characterization, optical properties

I. Introduction

ZnO-SiO$_2$ (Zn-Si oxide) composite systems, such as zinc silicate (Zn$_2$SiO$_4$), are functional inorganic materials with many promising applications, including photocatalysis [1,2], anti-corrosion [3], health protection [4], energy [5–7], optics [8], phosphors [9,10] and adsorbents [11–13]. Zn-Si composite systems can be fabricated using various methods, including sonochemical [1], hydrothermal [2], sol-gel [14] and solid-state methods [15], where silicone sources could be derived from commercial silicate compounds [9,16], biomass [8], natural mineral [6], or industrial tailing [12]. Among these sources, using natural sources in the fabrication of Zn-Si composite is promising due to being economically favourable, value-added and easily obtained. In addition, previous studies have revealed that the intrinsic properties of Zn-Si composite systems, including, but not limited to optical, electronic and structural properties, are significantly influenced by the temperature used during fabrication [9,13,17], which determines their potential application.

In fact, this study used a direct precipitation method to fabricate the Zn-Si oxide composite using rice husk

*Corresponding author: tel: +62 812 8853 0160
e-mail: oman003@brin.go.id*

ash (RHA)-derived Na_2SiO_3 as the silicon source. The structural characterization and the adsorptive and antimicrobial performance of the non-calcined (as-prepared) Zn-Si oxide composite are discussed and compared with the Zn-Si oxide composite obtained by calcining at 1000 °C.

II. Experimental

2.1. Materials

Zinc nitrate hexahydrate ($Zn(NO_3)_2 \cdot 4\,H_2O$, >99.5% purity) and sodium chloride (p.a., ACS, ISO) were purchased from Merck, KGaA, Darmstadt, Germany. Sulfuric acid (H_2SO_4, EMSURE 95–97% purity), NaOH (EMSURE 95–97% purity) and HCl (EMSURE 37% purity) were obtained from Merck, Supelco, Darmstadt, Germany. Nutrient agar (microbiology grade) was purchased from HIMEDIA, Pennsylvania, USA. Congo red (C6767, Dye content >35%) was purchased from Sigma-Aldrich, WGK, Germany. All chemicals were used without purification. Alkaline sodium silicate (Na_2SiO_3) solution was derived from rice husk ash (RHA) by adopting a procedure published elsewhere [18]. All experiments used ultra-pure water from a direct purification system (Milli-Q, Merck Millipore, MA, USA). The bacterial strains *Bacillus subtilis* (FNCC 0059), *Staphylococcus aureus* (FNCC 0043), *Escherichia coli* (FNCC 08159) and *Pseudomonas aeruginosa* (ARCC 9027) were obtained from the collection of the Gadjah Mada University, Yogyakarta, Indonesia.

2.2. Fabrication of Na₂SiO₃ solution

The rice husk ash (RHA) powder, with an average particle size of about 105 μm, was washed successively with 200 ml of 1.5 M HCl solution and ultrapure water and then oven-dried at 105 °C for 24 h. Subsequently, 20 g of the dried RHA powder and 200 ml of 2.5 M NaOH solution were mixed in a 250 ml beaker and heated at 80 °C for 2 h with continuous stirring. After that, the resulting Na_2SiO_3 solution was separated from the residual solids by filtration using Whatman Class 41 ashless filter paper. The obtained Na_2SiO_3 solution was denoted as RHA-Na_2SiO_3. X-ray fluorescence (XRF) testing showed that the SiO_2 isolated from RHA-Na_2SiO_3 had a purity of about 94% (detailed data not shown here).

2.3. Preparation of Zn-Si oxide composite systems

The Zn-Si oxide composite systems were prepared using the direct precipitation method. In a typical experiment, 20 ml of alkaline RHA-Na_2SiO_3 solution was transferred into a 100 ml beaker. The precipitation was carried out by dropwise adding a 2 M $Zn(NO_3)_2$ solution to an alkaline RHA-Na_2SiO_3 solution while stirring. A solid precipitate formed immediately upon adding $Zn(NO_3)_2$ solution, and the precipitation process continued until the mixture reached pH 7. The solid residue

was separated by centrifugation at 6000 rpm for 5 min and then washed using ultrapure water until a stable pH was reached. The washed solid residue was dried overnight at 105 °C, and the obtained dried solid was marked as APS (as-prepared sample). A certain amount of APS was calcined at 1000 °C in a furnace under atmospheric conditions for 3 h. The calcined sample was labelled as CS. Both APS and CS samples were kept in desiccators for further use in characterization and activity tests.

2.4. Characterization

Thermal analyser (TGA, STA PT 1600 Linseis Messgeraete, Selb, Germany) was used to evaluate physicochemical phenomena related to mass loss in a temperature range from 25 to 1100 °C at a heating rate of 10 °C/min, and the analyses were performed under a constant nitrogen flow at a rate of 5 l/h. An X-ray diffractometer (XRD, Rigaku SmartLab, Tokyo, Japan) using 40 kV and 30 mA Cu-Kα radiation ($\lambda = 1.542$Å) with continuous scanning mode was used to confirm the phase structure and crystallinity. The functional groups were recorded using a Fourier transform infrared spectrophotometer (FT-IR, Bruker Tensor II, MA, USA) displaying ATR in the 4000–400 cm^{-1} spectral range. N_2 adsorption-desorption was measured with a BET Tristar II analyser (Micromeritics Instrument Corporation, USA) under liquid nitrogen temperature (-196 °C) with relative pressure, P/P_0, ranging from 0.01 to 0.99. Photoluminescence (PL) signals were measured at room temperature using a picosecond laser with a 450 nm long-pass filter and a 60 W laser diode with excitation at $\lambda = 405$ nm. Absorption spectra of the samples were measured using a UV-Vis spectrophotometer (2450 Shimadzu, Japan) at a wavelength of 200–800 nm with $BaSO_4$ as the reference. Morphological images were captured using transmission electron microscopy (TEM) Talos F200X (Thermo Scientific, USA) operated at 200 kV and field emission scanning electron microscope (FESEM, JIB-4610F, Jeol, Tokyo, Japan), operated at 15 kV with gold coating.

2.5. Activity and antimicrobial tests

The activity test was a preliminary study to evaluate the ability of both APS and CS samples as adsorbents in removing textile dye from solution and as antimicrobial agents. The adsorption evaluation was performed by ultrasound-assisted adsorption (UAA) method using batch tests in an ultrasonic apparatus (Branson Bransonic®, Mechanical Bath 8800, Emerson, USA). Initially, a certain amount of APS or CS as adsorbents were put into a 50 ml vial containing a Congo red (CR) dye solution with known concentration and placed in the ultrasonic chamber to start the adsorption experiment. After a set adsorption period, specific volume of CR solution was collected. The treated CR solution was separated from the solid adsorbent by centrifugation at 6000 rpm for 5 min. The absorbance of

the treated CR solution was then measured using a UV-Vis spectrometer by scanning at a 200–600 nm wavelength. The residual CR concentration in the treated solutions was determined using a calibration curve equation ($Y = 0.0358X + 0.0158$, $R^2 = 0.9999$) derived from a series of CR standards with a known concentration (0–60 ppm). The adsorption efficiency (*AE*) of APS and CS in removing CR dye was calculated using following equation [19]:

$$AE = \frac{C_0 - C_t}{C_0} \cdot 100 \qquad (1)$$

where C_0 is initial CR concentration at $t = 0$ min and C_t is CR concentration at time t.

The total plate count (TPC) antimicrobial test was conducted by adopting the standard method of the American Public Health Association [20]. The test was performed under aseptic conditions using sterilized materials, except for the APS and CS. Typically, 400 µl of 85% NaCl, 100 µl bacterial isolates and 10 µg of the APS or CS were sequentially transferred into a 1.5 ml vial. The mixture was homogenized and incubated at 37 °C for 24 h. The incubated suspension (50 µl) was then added to the nutrient media using a pour plating technique, followed by incubation at 37 °C for 24 h. After incubation, the number of growing colonies was counted.

III. Results and discussion

3.1. Characterization

TGA/DSC analysis

Thermal analyses (TGA/DSC) are widely employed methods for assessing the thermal characteristics of materials [21]. The thermal behaviour of APS was studied in the range of 25–1100 °C, and the results are presented in Fig. 1. The TGA curve exhibits two stages of weight loss, while the DSC curve shows five exothermic peaks accompanied by two endothermic peaks. The first weight loss stage (29.67%) occurred at temperatures ranging from 25 to 450 °C, with three large exothermic peaks on the DSC curve. The exothermic peaks
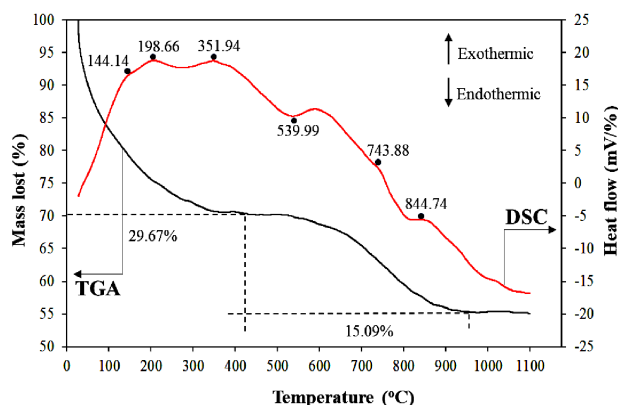

Figure 1. TGA-DSC pattern of APS

at 144.14 and 198.66 °C can be attributed to the dehydration and complete elimination of the physisorbed moisture [22,23]. This water removal occurs with the combustion of the remaining organic chemicals, indicated by a broad exothermic peak at 351.94 °C [24]. The second weight-loss stage of about 15.09% occurs in the temperature range 450–800 °C. This process is characterized by two exothermic peaks and one endothermic peak on the DSC curve. The exothermic peak at temperature 743.88 °C can be associated with dehydration and crystallization of metal oxide [22–25]. Other endothermic and exothermic peaks occur at 539.99 and 844.74 °C, respectively. Lin and Shen [25] and Marinović-Cincović *et al.* [26] found that temperatures at about 539.99 and 844.74 °C could be associated with metal oxide conversion and structural stability, respectively. It is worth noting that, however, in our study, TGA analysis demonstrated structural stability starting at higher temperatures (above 1000 °C). For this reason, 1000 °C was selected as the calcination temperature, and thus a complete conversion of SiO_2 and ZnO in the as-prepared sample to yield a stable Zn-Si oxide composite could be expected.

XRD analysis

X-ray powder diffraction (XRD) is an analysis technique for studying the phase and structure of materials [27]. Figure 2 depicts the APS and CS diffractograms. Phase analysis was carried out by refining the XRD diffractograms using a PDXL 2 version 2.8.4.0 software package (Rigaku Corporation) and matching each detected compound with the powder diffraction file (PDF-4+) card [28]. The XRD pattern of APS shows a characteristic of amorphous SiO_2 centred at 2θ values between 22–23° [9,18]. Nonetheless, some low intensity diffractions at 2θ of 23.54°, 25.02°, 26.91°, 28.5°, 29.99°, 32.91° and 38.12° were also observed, ascribing the reflection of $(13\bar{1})$, (002), (311), $(33\bar{1})$, (240), (240) and (312) crystal planes of silicon oxide (SiO_2, PDF card# 04-015-6254), respectively. The low diffraction intensity of SiO_2 in APS indicated that SiO_2 was present as a semi-crystalline phase. ZnO phase was also obviously observed in APS with diffractions at 2θ of 31.75°, 34.41°, 36.25° and 47.42° corresponding to reflections of (100), (002), (101) and (102) crystal planes, respectively. These reflection planes well matched with the hexagonal zincite structure with cell parameters $a = b = 3.2499$ Å and $c = 5.2066$ Å (PDF card# 04-009-7657). These results suggest that the used fabrication condition may promote a simultaneous formation of amorphous and semi-crystalline SiO_2.

In contrast with APS, the diffraction peaks intensities of CS (Fig. 2b) increase significantly, which implies increase in its crystallinity. Phase analysis shows that α-Zn_2SiO_4 is dominant phase, which is indicated by its characteristic high diffraction peaks (Fig. 2b), and belong to the hexagonal system of willemite structure with the cell parameters $a = b = 13.9480$ Å and $c = 9.3150$ Å
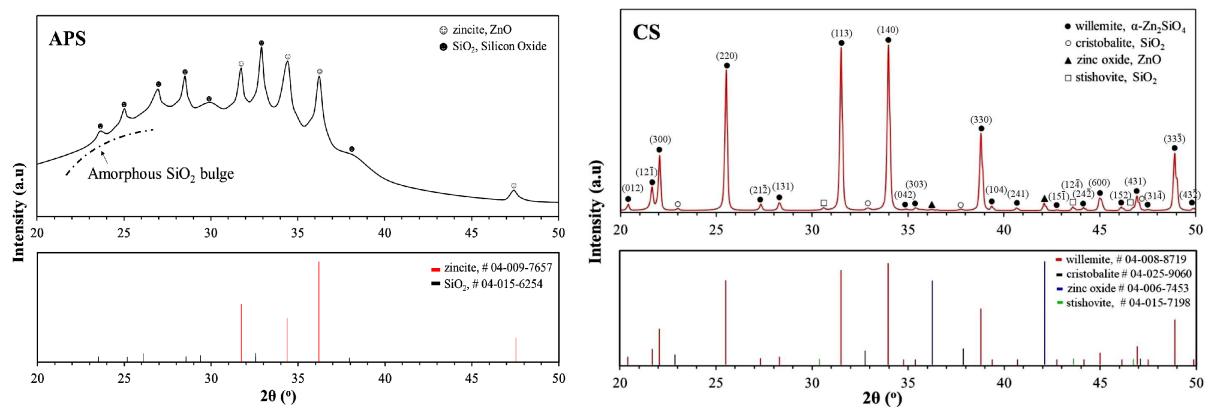
Figure 2. XRD patterns of APS (a) and CS (b)

(PDF card# 04-008-8719). Phase analysis also detected the presence of weak diffraction peaks of cristobalite, stishovite and zinc oxide. The phase structure of the cristobalite is indicated by the diffraction peaks at 2θ of 23.00°, 32.86°, 37.73° and 46.95°, ascribed to the reflections of (101), (102), (200) and (202) crystal planes, respectively, well corresponding to the tetragonal system of a cristobalite structure with cell parameters $a = b = 4.7900\text{ Å}$ and $c = 6.6500\text{ Å}$ (PDF card# 04-025-9060). Two diffraction peaks at 2θ of 30.60° and 43.93° can be ascribed to the reflections of (110) and (200) crystal planes of stishovite, respectively (PDF card# 4-015-7198), having a tetragonal system with cell parameters $a = b = 4.1485\text{ Å}$ and $c = 2.6620\text{ Å}$. Lastly, the zinc oxide in CS is characterized by two diffraction peaks at 2θ of 36.24° and 42.11°, respectively, all ascribed to the reflections of (111) and (200) crystal planes, respectively, of zinc oxide having a cubic system with cell parameter of $a = 4.2900\text{ Å}$, respectively (PDF card# 04-006-7453).

To further prove the crystallinity (%), diffractograms of APS and CS were analyzed, where the total area of crystalline peaks was divided by the entire (crystalline and amorphous peaks) area under the diffraction curve with the help of OriginPro SR1 (OriginLab Corporation, Northampton, MA, USA, 2018), yielding calculated crystallinities of about 23.3% and 96.5% for APS and CS, respectively. In addition, the Debye-Scherrer formula [19] was employed for crystallite size determination. The crystallite sizes of APS and CS differed greatly, with CS having a crystallite size of approximately 71.8 nm, nearly 4.5 times larger than APS (17.6 nm). These results show that high calcination temperatures improved CS particles' crystallinity and crystallite size compared to APS. Similar observations related to the impact of calcination temperature on crystallinity and crystallite size of metal oxides have been previously reported by Zaid *et al.* [9] and Pratibha *et al.* [17].

FT-IR analysis

FT-IR is a powerful method to identify key chemical structures and quantify the composition of materials using their distinctive vibrational absorption bands [29]. FT-IR spectra of APS and CS are presented in Fig. 3. Both spectra show several absorption bands characteristic of silicon and zinc oxide in wavenumbers range 400–1100 cm^{-1}. The spectrum of APS shows four absorption bands in range 400–1000 cm^{-1}. The absorption bands with sharp peaks at 421.54 and 484.93 cm^{-1} can be attributed to asymmetric stretching vibrations of inorganic ZnO [22,23]. The absorption bands with 518.49 and 955.45 cm^{-1} peaks are assigned to the ZnO symmetric stretching in the ZnO$_4$ group and SiO$_4$ asymmetric stretching vibration, respectively [30–32]. The absorption peaks detected in the APS spectrum were also clearly observed in the CS spectrum despite a noticeable shift towards lower wavenumbers. This occurrence can be attributed to the phase change and increase in the crystallinity of the metal oxide species due to the high-temperature treatment [32]. The calcination temperature also resulted in the disappearance of characteristic peaks
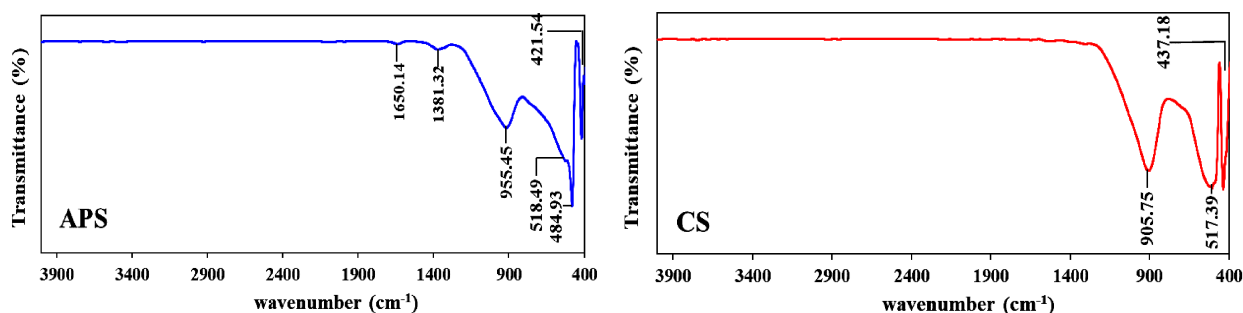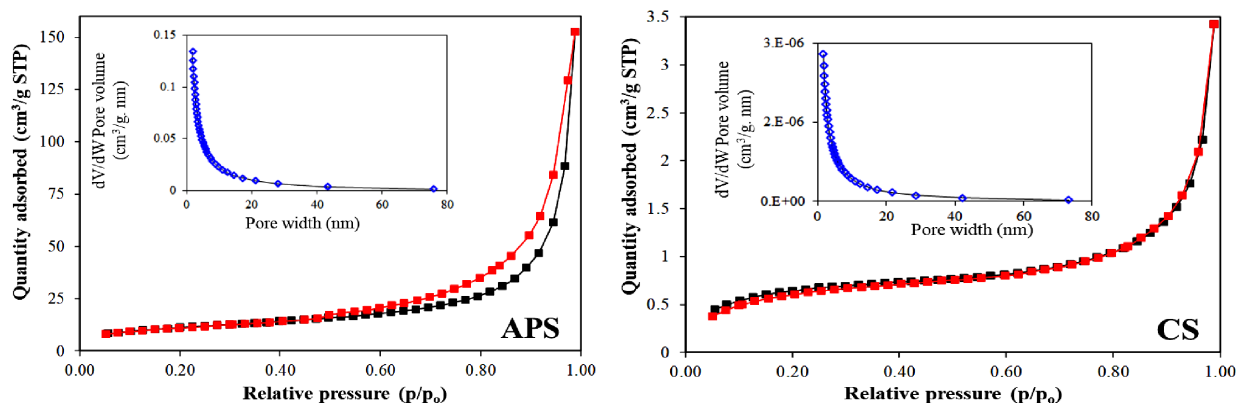

Figure 3. FT-IR spectra of APS (a) and CS (b)

Figure 4. N$_2$ adsorption-desorption isotherms of APS (a) and CS (b)

of physically adsorbed water on CS at wavenumbers of 1381.32 and 1650.40 cm^{-1} [33].

N$_2$ adsorption-desorption

Nitrogen adsorption-desorption is a widely used method to confirm the porosity of a material [34]. Nitrogen adsorption and desorption isotherms of APS and CS are shown in Fig. 4, along with their hysteresis loops character around P/P_0 values of 0.75–1.0. The isotherm of the APS sample exhibits adsorption isotherm type IV, indicating a characteristic mesoporous material [35,36]. The isotherm of APS exhibits a type H3 hysteresis ring [35], which may be caused by the roughness of its pore and particle surface. Moreover, the isotherm of the CS sample demonstrates a type II, which implies that the CS sample could be classified as non-porous material [37]. The surface characteristics, including specific surface area, the total pore volume and average pore size, were found to be 39.8 m^2/g, 0.000467 cm^3/g, 23.7 nm, and 2.2 m^2/g, 0.000153 cm^3/g, 9.6 nm for APS and CS, respectively. In other words, the surface characteristics values of CS are lower than those of the APS, with specific surface area, total pore volume and average pore size all decreasing by 94.4%, 67.2% and 59.7%, respectively. The significant drop in surface properties of CS is most likely attributable to the considerable collapse of pore structure caused by the calcination process at high temperatures [38].

UV-DRS and PL analysis

UV-diffuse reflectance spectroscopy (UV-DRS) is one of the most widely used techniques to investigate the electronic properties of metal oxides and their composites [39]. Figure 5a depicts the absorption spectra of APS and CS in the wavelength region of 200–800 nm. It can be observed that absorption profiles of APS and CS are very similar, with broad bands in the wavelength region below 400 nm. Also, the intensity of CS is lower than APS and tends to shift towards a higher wavelength in the violet region. This phenomenon is likely caused by a higher crystallinity of CS, as evidenced by TEM, FESEM, FTIR and XRD data, which is also consistent with Babu *et al.* [40] and Zaid *et al.* [9]. We can also utilize the absorption spectrum data of metal oxide to determine its energy band gap by applying the Kubelka-Munk function formula [19]. Figure 5b displays a plot between the Kubelka-Munk function and band gap energy (E_g) of APS and CS. The band gap energy of CS (3.26 eV) is found to be lower than for APS (3.29 eV). In particular, a high calcination temperature treatment causes redshift absorption towards higher wavelengths, indicating the band gap energy associated with the glass crystallization process [32].

Photoluminescence (PL) spectroscopy is a non-invasive and non-damaging technique used to investigate optical properties of materials [41]. The behaviour
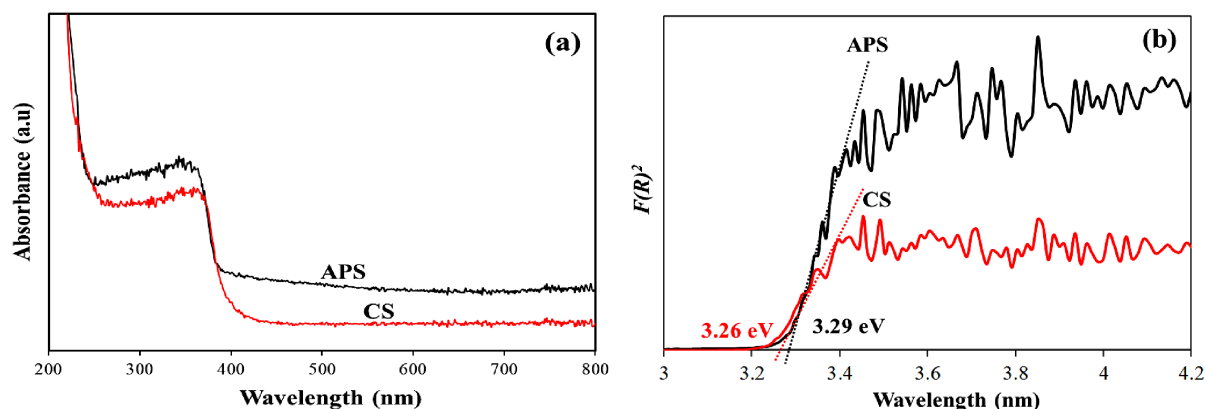

Figure 5. UV-DRS adsorption spectra (a) and band gap energy (b) of APS and CS
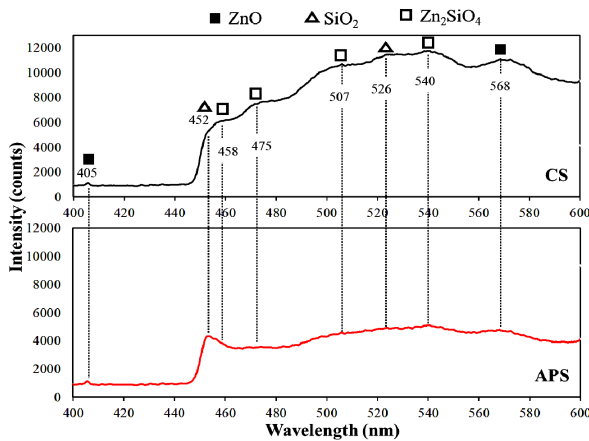
Figure 6. Photoluminescence spectra of APS and CS

of PL spectra of materials depends profoundly on the preparation method and the heat treatment given. Figure 6 depicts the PL spectra of APS and CS, measured at room temperature with an excitation wavelength of 405 nm. Figure 6 shows that the different temperature treatments applied to APS and CS resulted in changes in the intensity of the PL spectra observed. According to our prior XRD data, APS with small crystallite sizes is found to be a mixture of amorphous and semi-crystalline structures, whereas CS with large particle sizes corresponds to crystalline structures. Such morphological and structural distinctions have the potential to influence PL intensity. As a result, the high crystallinity of CS reduces non-radiative electron-hole recombination rates [9], resulting in higher CS intensities than APS. In addition, the emission bands at wavelength 405 nm with a similar intensity between APS and CS are attributable to free excitation recombination at the near-band edge of ZnO [42]. The emission peak at 452 nm may be caused by the presence of defect centres in SiO_2 due to the non-bridging of hole and oxy-

gen vacancy centres, while the emission peak at 526 nm may be caused by changes in crystallite size [43,44]. Peaks at 458, 475, 507 and 540 nm correspond to emissions from α-Zn_2SiO_4. The emission peaks at around 458 and 475 nm are attributed to the emission bands of electron transitions from interstitial Zn to the valence band and from the conduction band to oxygen defects, respectively [45,46]. The 507 and 540 nm wavelengths could be associated with zinc interstitial and electron transitions, respectively [9].

TEM and FESEM analyses

TEM and FESEM techniques have been widely used to examine the effect of temperature treatment on the morphology, shape and particle dispersion of materials [1,7,9]. The TEM of APS (Fig. 7) shows particles with an amorphous nature and no crystal arrangement, which is verified by its selected area electron diffraction (SAED) data that indicates halo ring patterns of non-crystal material. The HRTEM image of the APS shows a lattice fringe, which is characteristically a sign of a material in the crystalline phase. The *d*-spacing of lattice fringes was calculated using ImageJ [47] software and yielded a value of about 0.25 nm. This value is consistent with the *d*-spacing of (101) plane of hexagonal zincite (PDF card# 04-009-7657). In addition, the matching lattice fringes associated with SiO_2 crystal were not observable. This result suggests that the APS structure was not fully amorphous. Likely, APS has a pseudo-amorphous-like structure consisting of amorphous SiO_2 and ZnO crystals, which is confirmed by the visual appearance of the FESEM image in Fig. 8.

The TEM images of CS (Fig. 7) are characterized by morphology with interconnected fused-like particles. In contrast, the SAED image of CS shows a dotted pattern, which is a distinguishing feature of polycrystalline material. The FESEM image of CS in Fig. 8 clarifies such morphology with interconnected fused-like parti-
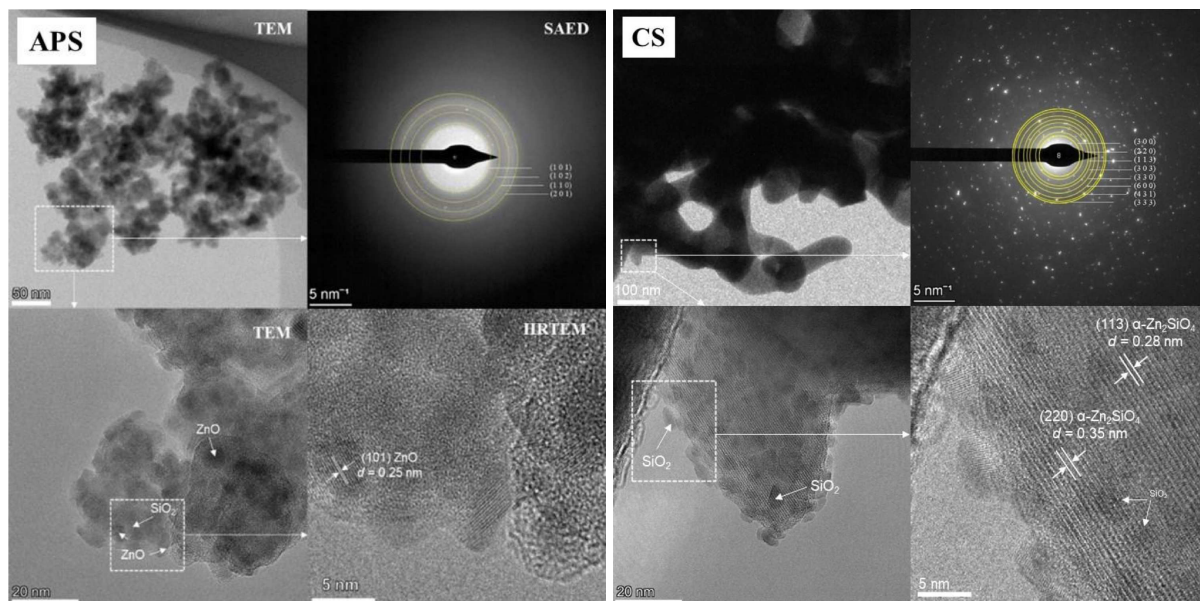

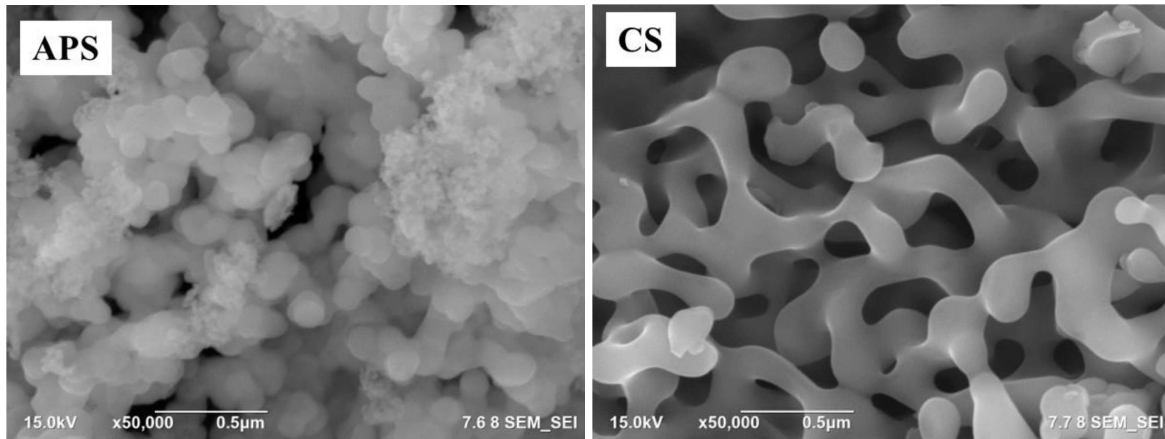**Figure 7. TEM-related images of APS (a) and CS (b)**

Figure 8. FESEM images of APS (a) and CS (b)

Table 1. Structural characteristic comparison of fabricated Zn-Si composite to those from previous similar studies

Method	Si-sources	Formation temperature	Particle shape	Phase	D [nm]	SA [m^2/g]	E_g [eV]	Ref.
hydrothermal	organic silicate	130 °C	nest-like and hollow structure	crystalline	30	n.a.	4.90	[2]
one-step hydrothermal	iron ore tailings	180 °C	flower-like structure	crystalline	n.a.	81.4	n.a.	[12]
sol-gel	tetraethyl ortosilicate	950 °C	powdered particle	crystalline	58.3	n.a.	n.a.	[14]
hydrothermal	SiO$_2$	220 °C	nanorod	crystalline	78.3	n.a.	5.05	[53,54]
one-pot sol-gel	tetraethyl ortosilicate	550 °C	rod-like	amorphous	n.a.	292	n.a.	[50]
solid state	SiO$_2$ powder	900 °C	n.a.	crystalline	297	n.a.	5.05	[55]
precipitation	RHA	1000 °C	interconnected fused-like structure	crystalline	71.8	2.2	3.26	This work

n.a. – not available

cles of CS. Lattice fringe calculation of the HRTEM image results in d-spacing values of about 0.28 and 0.35 nm, associated with reflection of (113) and (220) crystal planes, respectively. These two d-spacing values are closely related to hexagonal α-Zn$_2$SiO$_4$ (PDF card# 04-008-8719) with space group: $R\bar{3}$ (148) having cell parameters of $a = b = 13.9480$ Å, $c = 9.3150$ Å. Furthermore, careful examination of lattice fringes and lattice spacing positions, on both SAED and HRTEM of CS images (Fig. 7), can infer that most likely CS particles consist of α-Zn$_2$SiO$_4$ compound surrounded by SiO$_2$-particles with well-defined boundaries. This result is confirmed by the XRD data, which implies the presence of the SiO$_2$/α-Zn$_2$SiO$_4$ composite in CS particles.

Table 1 compares the fabricated Zn-Si composite to those from previous similar studies. As seen in Table 1, our method could produce particles with unique shapes that are different from previous similar studies with comparable crystal sizes. This structural condition could further impact its adsorbent and antimicrobial agent performance. Besides, a relatively lower band gap value implies that the Zn-Si composite may absorb a broader range of light, showing potential to work under visible light radiation.

3.2. Activity studies

Dye adsorption test

Several parameters, including adsorbate concentration, adsorbent weight, solution pH and adsorption time, may influence the adsorbent's ability to remove adsor-
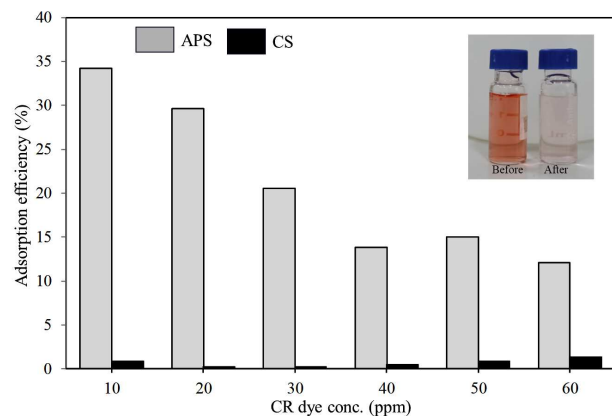

Figure 9. Adsorption efficiency of APS and CS in CR removal at various concentrations (insert: 10 ppm CR solution before and after adsorption at 30 °C, solution pH = 5 and adsorbent concentration of 0.5 g/l)

bate from the solution [48,49]. The efficiency of APS and CS as adsorbents in removing dyes was tested using Congo red (CR) as a model. In this preliminary test, the abilities of APS and CS as adsorbents were evaluated as a function of CR concentration (Fig. 9). As it can be seen, APS exhibits a much higher efficiency in CR removal than CS, while it decreases with increasing CR concentration. In the former case, the increased effectiveness of APS over CS could be attributable to surface features. APS with a higher surface area is expected to have more active sites on its surface, allowing for a stronger interaction between the APS and CR molecules in the solution. In the latter case, raising the concentration of CR may increase the number of adsorbate molecules in the solution that interact with the active
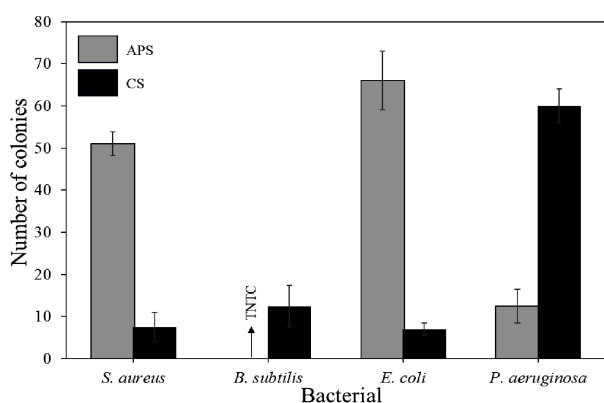
sites on the APS surface, resulting in inadequate number of surface-active sites to adsorb entire CR molecules. Previous studies have also revealed that the structural properties of Zn-Si composite play an important role in their adsorptive performance for toxic substance removal [11–13,50,51].

Antimicrobial test

Total plate count (TPC) method was performed to assess the inhibitory effects of APS and CS on the growth of gram-positive bacteria (*S. aureus* and *B. subtilis*) and gram-negative (*E. coli* and *P. aeruginosa*) bacteria. Figures 10 and 11 provide statistical and visual data from the TPC experiment, respectively. Both data show more colonies of *S. aureus*, *B. subtilis* and *E. coli* in the nutrient media treated with APS than with CS, except for *P. aeruginosa*. These findings indicate that CS is more effective than APS in preventing bacterial growth under the experimental conditions used in this study. It is commonly acknowledged that surface characteristics of metal oxides can influence their interaction with cell walls, influencing the degree of efficacy in inhibiting bacterial growth [52]. APS with a high specific surface area ($39.8\,cm^2/g$) has a lower inhibitory power than CS ($2.2\,cm^2/g$), suggesting that surface area was not a determining factor. In other words, CS with interconnected fused-like particles is more effective in inhibiting microbial growth (Fig. 10). It could be used as evidence that the architecture of the Zn-Si composite plays an important role in controlling the microbial growth rate. The voids among interconnected fused-like particles of

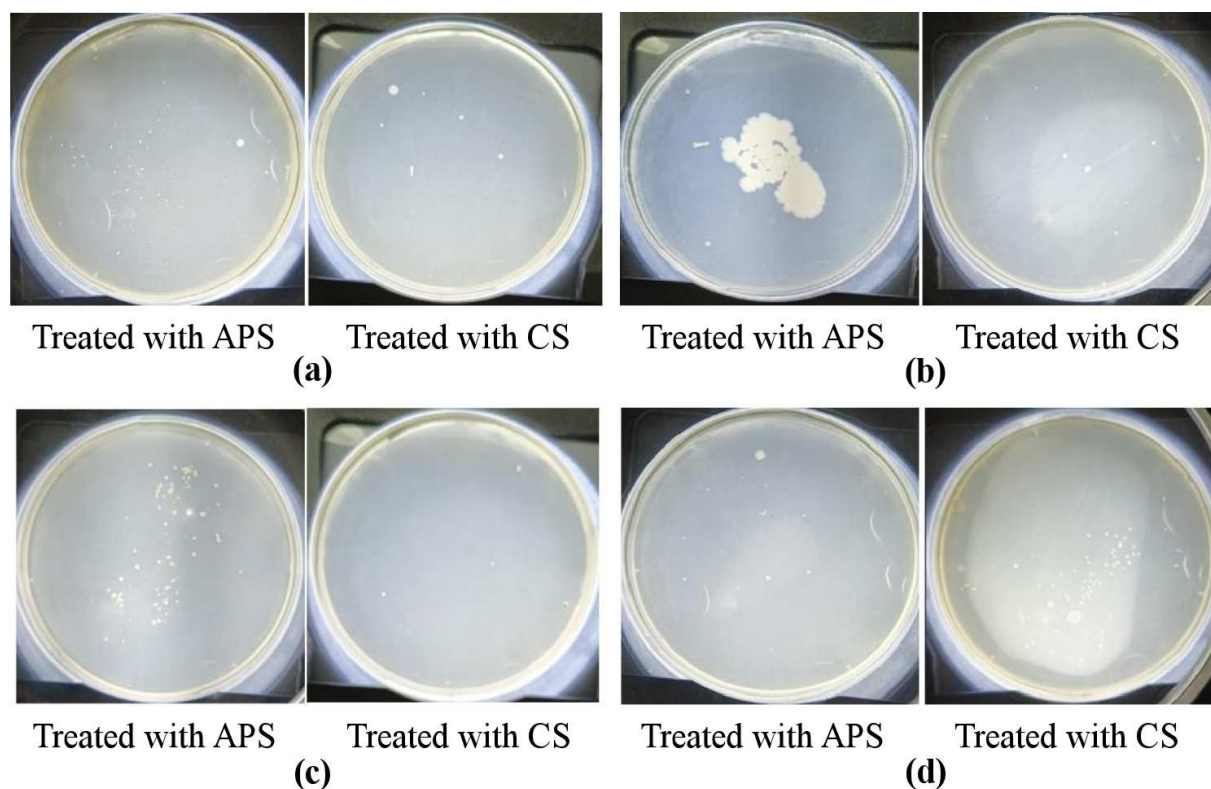**Figure 10. Number of growing colonies after incubation at 37 °C for 24 h (results are mean of two TPC)**

Figure 11. Visual data of bacterial colonies of *S. aureus* (a), *B. subtilis* (b), *E. coli* (c) and *P. aeruginosa* (d) grown in nutrient media treated with APS and CS during TPC assay

CS particles (Fig. 8) may facilitate the interaction between the CS particle and microbial cell walls. Jindal *et al.* [50] discovered that the ability of zinc silicate biocomposite to inhibit *S. Aureus* might be attributed to the release of zinc ions and the interaction between the particle surface and the microbial cell walls.

IV. Conclusions

Zn-Si oxide composite was successfully prepared using a simple precipitation method. Calcination treatment at high temperatures affected the morphological and structural characteristics of the composite. Calcination increased the crystallinity degree and crystallite sizes, decreasing surface characteristics (such as specific surface area, total pore volume and average pore size), shifting the FT-IR vibration mode positions towards lower wavenumbers and increasing PL intensity. The as-prepared sample (APS) exists as a ZnO/SiO_2 composite consisting of amorphous SiO_2 and ZnO zincite crystals with a pseudo-amorphous structure. The calcined sample (CS) is dominated by willemite α-Zn_2SiO_4, along with low amounts of cristobalite, zinc oxide and stishovite. The CS exists as SiO_2/α-Zn_2SiO_4 composite with a polycrystalline structure. According to preliminary dye adsorption and antimicrobial activity evaluations, our composites demonstrate their adsorptive properties on Congo red removal and pathogenic bacteria inhibition. Nonetheless, more research on process optimization is needed, considering the effects of numerous experimental conditions, such as the use of light in absorption and antimicrobial investigations, among others.

References

1. M. Masjedi-Arani, M. Salavati-Niasari, "A simple sonochemical approach for synthesis and characterization of Zn_2SiO_4 nanostructures", *Ultrasonics Sonochem.*, **29** (2016) 226–235.
2. Z. Qiao, T. Yan, X. Zhang, C. Zhu, W. Li, B. Huang, "Low-temperature hydrothermal synthesis of Zn_2SiO_4 nanostructures and the novel photocatalytic application in wastewater treatment", *Catal. Commun.*, **106** (2018) 78–81.
3. Z.-L. Chai, Y.-X. Chen, D. Zhou, M. Zhang, J.-K. Liu, "Excellent corrosion resistance of FGO/Zn_2SiO_4 composite material in epoxy coatings", *Prog. Organ. Coatings*, **170** (2022) 106992.
4. M. Saberi Rise, A. Hosseini Ranjbar, H. Noori, V. Saheb, "Synthesis and characterization of ZnO nanorods-Zn_2SiO_4 nanoparticles-PMMA nanocomposites for UV-C protection", *Optical Mater.*, **123** (2022) 111922.
5. P. Diana, S. Sebastian, S. Saravanakumar, M.C. Robert, M. Shkir, "Sol-gel synthesized rare earth La^{3+} ions doped Zn_2SiO_4 phosphors for lighting applications", *Ceram. Int.*, **49** [16] (2023) 26469–26478.
6. Y. Li, L. Huang, J. Peng, Y. Wu, "Interfacial ionic conductivity of two-dimensional heterogeneous semiconductor ZnO composited with Zn_2SiO_4 derived from natural clay mineral vermiculite", *Ceram. Int.*, **48** [21] (2022) 32436–32443.
7. S. Zhang, M. Lu, Y. Li, F. Sun, J. Yang, S. Wang, "Synthesis and electrochemical properties of Zn_2SiO_4 nano/mesorods", *Mater. Lett.*, **100** (2013) 89–92.
8. S.A.A. Wahab, K.A. Matori, M.H.M. Zaid, M.M.A. Kechik, N. Effendy, R.E.M. Khaidir, "Blue emission: Optical properties of Co^{2+} doping towards Zn_2SiO_4 glass-ceramics", *Optik*, **274** (2023) 170528.
9. M.H.M. Zaid, K.A. Matori, Y. Yaakob, I.M. Alibe, "Simple thermal treatment approach for the synthesis of α-Zn_2SiO_4 nanoparticles", *Optics Laser Technol.*, **140** (2021) 106991.
10. C.-C. Diao, C.-F. Yang, R.-L. Wang, J.-J. Lin, M.-Y. Fu, "Prepare high efficiency Mn^{2+}-doped Zn_2SiO_4 green phosphors in air using nano-particles", *J. Luminescence*, **131** [5] (2011) 915–920.
11. X. Wang, H. Huang, B. Liu, B. Liang, C. Zhang, Q. Ji, D. Chen, G. Shen, "Shape evolution and applications in water purification: The case of CVD-grown Zn_2SiO_4 straw-bundles", *J. Mater. Chem.*, **22** [12] (2012) 5330–5335.
12. G. Dong, G. Tian, L. Gong, Q. Tang, M. Li, J. Meng, J. Liang, "Mesoporous zinc silicate composites derived from iron ore tailings for highly efficient dye removal: Structure and morphology evolution", *Micropor. Mesopor. Mater.*, **305** (2020) 110352.
13. S. Tripathi, R. Bose, A. Roy, S. Nair, N. Ravishankar, "Synthesis of hollow nanotubes of Zn_2SiO_4 or SiO_2: Mechanistic understanding and uranium adsorption behavior", *ACS Appl. Mater. Interfaces*, **7** [48] (2015) 26430–26436.
14. B. Chandra Babu, S. Buddhudu, "Dielectric properties of willemite α-Zn_2SiO_4 nano powders by sol-gel method", *Phys. Procedia*, **49** (2013) 128–136.
15. M.Y. Yeh, C.C. Tu, S.H. Chang, S.Y. Lee, "Investigation on the fluorescent efficiency of Zn_2SiO_4:Mn synthesized by repeated solid-state sintering", *Modern Phys. Lett. B*, **36** [18] (2022) 2242034.
16. M. Benchikhi, R. Hattaf, A. Moutaabbid, R. El Ouatib, "Structural, morphological, and optical properties of Co- substituted Zn_2SiO_4 nanopowders prepared by a hydrothermal-assisted sol-gel process", *Mater. Chem. Phys.*, **276** (2022) 125434.
17. K. Pratibha, Chitralekha, H. Kaur, S. Shankar, S. Gaurav, Y. Dwivedi, "Influence of annealing temperature on structural, optical and electrical properties of zinc silicate (Zn_2SiO_4) nanophosphors", *Phys. B Condensed Matter*, **658** (2023) 414836.
18. J.B. Haider, M.I. Haque, M. Hoque, M.M. Hossen, M. Mottakin, M.A. Khaleque, M.A.H. Johir, J.L. Zhou, M.B. Ahmed, M. Zargar, "Efficient extraction of silica from openly burned rice husk ash as adsorbent for dye removal",

J. Cleaner Product., **380** (2022) 135121.

19. O. Zuas, H. Abimanyu, W. Widayanti, "Synthesis and characterization of nanostructured CeO$_2$ with dyes adsorption property", *Process. Appl. Ceram.*, **8** [1] (2014) 39–46.

20. APHA, Compendium of methods for the microbiological examination of foods, American Public Health Association, Washington DC, 2001.

21. J. Yang, N. Hedin, "Advances of lab-scale analytical methods for solidification/stabilization technologies", Ch. 29, pp. 483–495 in *Low Carbon Stabilization and Solidification of Hazardous Wastes*, Eds. D.C.W. Tsang, L. Wang, Elsevier, 2022,.

22. A.V. Blinov, A.A. Blinova, A.A. Kravtsov, A.A. Gvozdenko, A.V. Kobina, E.V. Momot, "Synthesis of multicomponent systems based on silicon dioxide and noble metal nanoparticles", *AIP Conf. Proceed.*, **2188** (2019) 040011.

23. Z.N. Kayani, F. Saleemi, I. Batool, "Effect of calcination temperature on the properties of ZnO nanoparticles", *Appl. Phys. A*, **119** [2] (2015) 713–720.

24. B. Chandra Babu, S. Buddhudu, "Structural and photoluminescence properties of Zn$_2$SiO$_4$:Tb^{3+} and Zn$_2$SiO$_4$:Tb^{3+}+Li$^+$ phosphors", *AIP Conf. Proceed.*, **1512** [1] (2013) 1292–1293.

25. C.-C. Lin, P. Shen, "Sol-gel synthesis of zinc orthosilicate", *J. Non-Crystal. Solids*, **171** [3] (1994) 281–289.

26. M. Marinović-Cincović, B. Janković, B. Milićević, Ž. Antić, R.K. Whiffen, M.D. Dramićanin, "The comparative kinetic analysis of the non-isothermal crystallization process of Eu^{3+} doped Zn$_2$SiO$_4$ powders prepared via polymer induced sol-gel method", *Powder Technol.*, **249** (2013) 497–512.

27. A. Pandey, S. Dalal, S. Dutta, A. Dixit, "Structural characterization of polycrystalline thin films by X-ray diffraction techniques", *J. Mater. Sci. Mater. Electron.*, **32** [2] (2021) 1341–1368.

28. S. Gates-Rector, T. Blanton, "The powder diffraction file: A quality materials characterization database", *Powder Diffraction*, **34** [4] (2019) 352–360.

29. A. Dutta, "Fourier transform infrared spectroscopy", Ch. 4, pp. 73–93 in *Spectroscopic Methods for Nanomaterials Characterization*, Eds. S. Thomas, R. Thomas, A.K. Zachariah, R.K. Mishra, Elsevier, 2017.

30. B. Satbaev, S. Yefremova, A. Zharmenov, A. Kablanbekov, S. Yermishin, N. Shalabaev, A. Satbaev, V. Khen, "Rice husk research: From environmental pollutant to a promising source of organo-mineral raw materials, *Materials*, **14** [15] (2021) 4119.

31. M. Laad, R. Datkhile, S. Shanmugan, "Synthesis and characterization of powder silica: A judicious recycling of the natural ceramic rice husk ash", *Silicon*, **14** [3] (2022) 1123–1132.

32. N.A.S. Omar, Y.W. Fen, K.A. Matori, M.H.M. Zaid, M.R. Norhafizah, M. Nurzilla, M.I.M. Zamratul, "Synthesis and optical properties of europium doped zinc silicate prepared using low cost solid state reaction method", *J. Mater. Sci. Mater. Electron.*, **27** [2] (2016) 1092–1099.

33. H.H. Ali, H.H. Mihsen, K.A. Hussain, "Synthesis, characterization and antimicrobial studies of modified silica materials derived from rice husks", *BioNanoScience*, **13** [3] (2023) 1163-1176.

34. K. Sing, "The use of nitrogen adsorption for the characterisation of porous materials", *Colloids Surfaces A*, **187-188** (2001) 3–9.

35. M. Thommes, "Physisorption of gases, with special reference to the evaluation of surface area and pore size distribution (IUPAC Technical Report)", *Chem. Inter.*, **38** [1] (2016) 25.

36. Z.A. Alothman, "A review: Fundamental aspects of silicate mesoporous materials", *Materials*, **2021** (2012) 2874–2902.

37. F. Ambroz, T.J. Macdonald, V. Martis, I.P. Parkin, "Evaluation of the BET theory for the characterization of meso and microporous MOFs", *Small Methods*, **2** [11] (2018) 1800173.

38. R. Rashid, F. Afroze, S. Ahmed, M. Shah Miran, A. Bin, H. Susan, "Control of the porosity and morphology of ordered mesoporous silica by varying calcination conditions", *Mater. Today Proceed.*, **15** (2019) 546–554.

39. Z. Yang, M. Zhu, "Case studies: Ultraviolet-visible (UV-Vis) spectroscopy", pp. 265–283 in *Springer Handbook of Advanced Catalyst Characterization*, Eds. I.E. Wachs, M.A. Bañares, Springer International Publishing, Cham, 2023.

40. B. Chandra Babu, B.V. Rao, M. Ravi, S. Babu, "Structural, microstructural, optical, and dielectric properties of Mn^{2+}: Willemite Zn$_2$SiO$_4$ nanocomposites obtained by a sol-gel method", *J. Mol. Struct.*, **1127** (2017) 6–14.

41. J.T. Torvik, "Dopants in GaN", Ch. 2, pp. 17–49 in *III-Nitride Semiconductors: Electrical, Structural and Defects Properties*, Ed. O. Manasreh, Elsevier, Amsterdam, 2000.

42. A.-T.T. Do, H.T. Giang, T.T. Do, N.Q. Pham, G.T. Ho, "Effects of palladium on the optical and hydrogen sensing characteristics of Pd-doped ZnO nanoparticles", *Beilstein J. Nanotechnol.*, **5** (2014) 1261–1267.

43. S. Roushdey, "Defect related luminescence in silicon dioxide network: A review", Ch. 8, in *Crystalline Silicon*, Ed. B. Sukumar, IntechOpen, Rijeka, 2011.

44. L.F. Koao, H.C. Swart, R.I. Obed, F.B. Dejene, "Synthesis and characterization of Ce^{3+} doped silica (SiO$_2$) nanoparticles", *J. Luminescence*, **131** [6] (2011) 1249–1254.

45. X.D. Gao, X.M. Li, W.D. Yu, "Synthesis and optical properties of ZnO nanocluster porous films deposited by modified SILAR method", *Appl. Surf. Sci.*, **229** [1] (2004) 275–281.

46. H. Chen, J. Ding, W. Guo, G. Chen, S. Ma, "Blue-green emission mechanism and spectral shift of Al-doped ZnO films related to defect levels", *RSC Adv.*, **3** [30] (2013) 12327–12333.

47. C.A. Schneider, W.S. Rasband, K.W. Eliceiri, "NIH Image to ImageJ: 25 years of image analysis", *Nat. Methods*, **9** [7] (2012) 671–675.

48. H. Budiman, O. Zuas, "Adsorption isotherm studies on acid orange-10 dye removal using cerium dioxide nanoparticles", *Indon. J. Chem.*, **14** [3] (2014) 226–232.

49. M.T. Yagub, T.K. Sen, S. Afroze, H.M. Ang, "Dye and its removal from aqueous solution by adsorption: A review", *Adv. Colloid Interface Sci.*, **209** (2014) 172–184.

50. A. Jindal, S. Juneja, M. Bakshi, P. Chaudhuri, J. Bhattacharya, "Mesoporous zinc silicate bio-composite: Preparation, characterization and in vitro evaluation", *Micropor. Mesopor. Mater.*, **277** (2019) 124–131.

51. D. Li, Y. Sun, Y.-L. Yang, X.-L. Shi, D.-A. Xie, L. Nie, J.-G. Chen, Z. Luo, H.-J. Chen, C.-A. Yang, Z.-G. Chen, "Converting industrial waste into valuable Zn$_2$SiO$_4$/SiO$_2$ nanosheets for highly effective organic dye removal", *Sustain. Mater. Technol.*, **39** (2024) e00834.

52. A. Raghunath, E. Perumal, "Metal oxide nanoparticles as antimicrobial agents: a promise for the future", *Int. J. Antimicrob. Agents*, **49** [2] (2017) 137–152.

53. D.K. Bharti, M.K. Gupta, A.K. Srivastava, "Temperature dependent dielectric and electric properties of zinc silicate nanorods", *Nano-Struct. Nano-Objects*, **17** (2019) 123–128.

54. D.K. Bharti, M.K. Gupta, A.K. Srivastava, "Giant dielectric constant and band gap reduction in hydrothermal grown highly crystalline zinc silicate nanorods", *Mater. Lett.*, **232** (2018) 66–69.

55. G. Essalah, G. Kadim, A. Jabar, R. Masrour, M. Ellouze, H. Guermazi, S. Guermazi, "Structural, optical, photoluminescence properties and Ab initio calculations of new Zn_2SiO_4/ZnO composite for white light emitting diodes", *Ceram. Int.*, **46** [8, Part B] (2020) 12656–12664.